

Correction

EARTH, ATMOSPHERIC, AND PLANETARY SCIENCES

Correction for “Improved El Niño forecasting by cooperativity detection,” by Josef Ludescher, Avi Gozolchiani, Mikhail I. Bogachev, Armin Bunde, Shlomo Havlin, and Hans Joachim Schellnhuber, which appeared in issue 29, July 16, 2013, of *Proc Natl Acad Sci USA* (110:11742–11745; first published July 1, 2013; 10.1073/pnas.1309353110).

The authors note that: “Due to a minor technical error in the calculation of the climatological average of the considered atmospheric temperatures for each calendar day, Figs. 2 and 3 appeared incorrectly. The amended figures and their legends are provided below. The main message and the interpretation of our paper remain unaffected by this correction.”

“The figures in the *Supporting Information* have been exchanged accordingly. We’d like to add that for the calculation of the climatological average, the leap days have been removed, and in the prediction phase, only the data from the past up to the prediction date have been considered. In addition, we note that for calculating the link strengths $S_{ij}(t)$, not the cross-covariance function $C_{ij}^{(i)}(\tau)$ has been considered but the absolute values of the corresponding cross-correlation functions $c_{ij}^{(i)}(\tau)$. When averaging over all link strengths, we obtain the time dependent average link strength $S(t)$. In the learning phase, we compare $S(t)$ with decision thresholds above its mean to obtain the optimal threshold used in the prediction phase.”

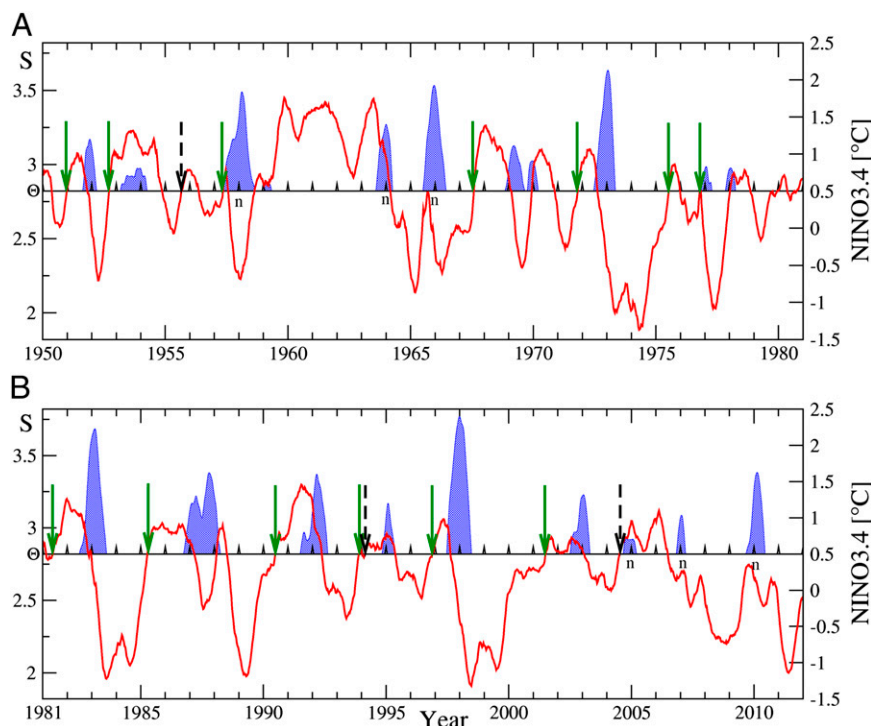


Fig. 2. The forecasting algorithm. We compare the average link strength $S(t)$ in the climate network (red curve) with a decision threshold Θ (horizontal line, here $\Theta = 2.82$) (left scale) with the standard NINO3.4 index (right scale), between January 1, 1950 and December 31, 2011. Only thresholds above the average of $S(t)$ in the learning phase are considered. When the link strength crosses the threshold from below outside an El Niño episode, we give an alarm and predict that an El Niño episode will start in the following calendar year. The El Niño episodes (when the NINO3.4 index is above 0.5°C for at least 5 mo) are shown by the filled blue areas. The first half of the record (A) is the learning phase where we optimize the decision threshold. In the second half (B), we use the threshold obtained in (A) to predict El Niño episodes. Correct predictions are marked by green arrows and false alarms by dashed arrows. The index n marks a nonpredicted El Niño episode. To resolve by eye the accurate positions of the alarms, we show in *SI Appendix*, Fig. S5, magnifications of those parts of Fig. 2 where the crossings or non-crossings are difficult to see clearly without magnification. We also show the alarms for the slightly larger threshold $\Theta = 2.83$ (*SI Appendix*, Fig. S6), which yields the same performance in the learning phase and one more false alarm in the prediction phase. The lead time between the prediction and the beginning of the El Niño episodes is 1.01 ± 0.28 y, while the lead time to the maximal NINO3.4 value is 1.35 ± 0.47 y.

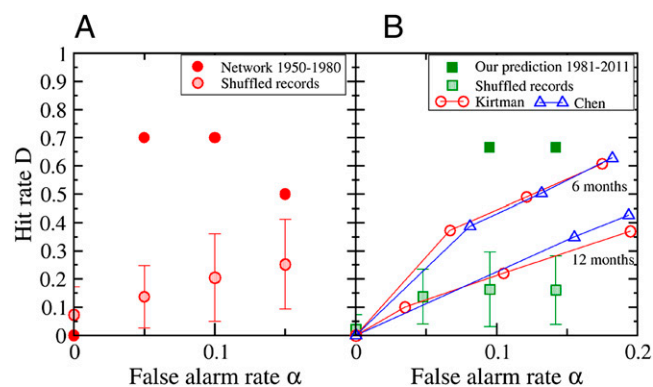


Fig. 3. The prediction accuracy [Receiver Operating Characteristic (ROC)-type analysis]. (A) For the four lowest false-alarm rates $\alpha = 0, 0.05, 0.1$, and 0.15 , the best hit rates D in the learning phase (Fig. 2A). The best result is obtained at $\alpha = 0.05$, where $D = 0.7$ and the decision threshold θ is between 2.815 and 2.834 . The results for the randomized $S(t)$ with error bars are shown by the shaded circles. (B) The quality of the prediction in the second half of the record, when the above thresholds are applied. For $2.815 < \theta \leq 2.826$, we have $D = 0.667$ at $\alpha = 0.095$, for $2.826 < \theta \leq 2.834$, we have $D = 0.667$ at $\alpha = 0.143$. For comparison, we show also results for 6- and 12-mo forecasts based on climate models (21, 37). The shaded squares and the error bars denote the mean hit rates and their SDs for predictions based on the shuffled data.

www.pnas.org/cgi/doi/10.1073/pnas.1317354110

Improved El Niño forecasting by cooperativity detection

Josef Ludescher^a, Avi Gozolchiani^b, Mikhail I. Bogachev^{a,c}, Armin Bunde^a, Shlomo Havlin^b, and Hans Joachim Schellnhuber^{d,e,1}

^aInstitut für Theoretische Physik, Justus-Liebig-Universität Giessen, 35392 Giessen, Germany; ^bDepartment of Physics, Bar-Illan University, Ramat Gan 52900, Israel; ^cRadio Systems Department, St. Petersburg Electrotechnical University, St. Petersburg 197376, Russia; ^dPotsdam Institute for Climate Impact Research, 14412 Potsdam, Germany; and ^eSanta Fe Institute, Santa Fe, NM 87501

Contributed by Hans Joachim Schellnhuber, May 30, 2013 (sent for review March 12, 2013)

Although anomalous episodic warming of the eastern equatorial Pacific, dubbed El Niño by Peruvian fishermen, has major (and occasionally devastating) impacts around the globe, robust forecasting is still limited to about 6 mo ahead. A significant extension of the prewarning time would be instrumental for avoiding some of the worst damages such as harvest failures in developing countries. Here we introduce a unique avenue toward El Niño prediction based on network methods, inspecting emerging teleconnections. Our approach starts from the evidence that a large-scale cooperative mode—linking the El Niño basin (equatorial Pacific corridor) and the rest of the ocean—builds up in the calendar year before the warming event. On this basis, we can develop an efficient 12-mo forecasting scheme, i.e., achieve some doubling of the early-warning period. Our method is based on high-quality observational data available since 1950 and yields hit rates above 0.5, whereas false-alarm rates are below 0.1.

climate | cross-correlations | dynamic networks | ENSO | spring barrier

The so-called El Niño-Southern Oscillation (ENSO) is the most important phenomenon of contemporary natural climate variability (1–4). It can be perceived as a self-organized dynamical see-saw pattern in the Pacific ocean-atmosphere system, featured by rather irregular warm (El Niño) and cold (La Niña) excursions from the long-term mean state. ENSO has considerable influence on the climatic and environmental conditions in its core region, but affects also distant parts of the world. The pattern is causing disastrous flooding in countries like Peru and Ecuador as well as heavy droughts in large areas of South America, Indonesia, and Australia. It is arguably also associated with severe winters in Europe, anomalous monsoon dynamics in East Asia, intensity of tropical cyclones such as hurricanes in the Caribbean, and epidemic diseases occurring in a variety of places (5–9).

Strong El Niño events, in particular, have affected, time and again, the fate of entire societies. A popular, yet quite informative account of ENSO's destructive power is provided in ref. 10. This book investigates the pertinent droughts in India, China, and Brazil toward the end of the 19th century, which killed an estimated 30–50 million people.

What happened in premodern times is unlikely to be repeated in the future. However, anthropogenic global warming (11, 12) may have a significant effect on the character of ENSO and render this geophysical pattern even more challenging for certain societies. In fact, the phenomenon is listed among the so-called “tipping elements” in the Earth System (13, 14) that might be transformed—sooner or later—by the greenhouse-gas emissions from fossil-fuel burning and land-cover change. The scientific jury is still out, pondering the question of how El Niño events will behave in a world without aggressive climate-protection measures (15). Will the eastern tropical Pacific warm permanently, periodically, or as irregularly as nowadays? Will the oscillation go away completely (something that appears rather unlikely according to the recent assessment by Wang et al. in ref. 4) or gain in strength (as suggested by some paleo-climatic data)? In the latter case, anything

that helps to improve the predictive power of the scientific ENSO analysis would be even more important than it is already today.

The ENSO phenomenon is currently tracked and quantified, for example, by the NINO3.4 index, which is defined as the average of the sea-surface temperature (SST) anomalies at certain grid points in the Pacific (Fig. 1). An El Niño episode is said to occur when the index is above 0.5 °C for a period of at least 5 mo. Sophisticated global climate models taking into account the atmosphere–ocean coupling as well as dynamical systems approaches, autoregressive models, and pattern-recognition techniques applied on observational and reconstructed records have been used to forecast the pertinent index with lead times between 1 and 24 mo. Up to 6 mo, the various forecasts perform reasonably well, whereas for longer lead times the performance becomes rather low (16–29). A particular difficulty for prediction of the NINO3.4 index is the “spring barrier” (see, e.g., ref. 30). During boreal springtime, anomalies that develop randomly in the western Pacific reduce the signal-to-noise ratio for the dynamics relevant to ENSO and make it harder to predict across the barrier.

In this study, we follow a different route. Instead of considering the time dependence of climate records at single grid points i , we study the time evolution of the interactions (teleconnections) between pairs of grid points i and j , which are represented by the strengths of the cross-correlations between the climate records at these sites. The interactions can be considered as links in a climate network where the nodes are the grid points (31–34). Recent empirical studies have shown that in the large-scale climate network the links tend to weaken significantly during El Niño episodes, and this phenomenon is most pronounced for those links that connect the “El Niño basin” (solid circles in Fig. 1) with the surrounding sites in the Pacific ocean (open symbols in Fig. 1) (the El Niño basin considered here consists of the NINO1, NINO2, NINO3, and NINO3.4 regions plus one grid point south of the NINO3.4 region) (32, 33).

Therefore, we concentrate on these links and show that well before an El Niño episode their mean strength tends to increase. We use this robust observation to forecast El Niño development more than 1 y in advance. We use the time span between 1950 and 2011, where the information on ENSO dynamics is reliable and the observational data necessary for constructing the climate network are complete (35).

We use the network shown in Fig. 1, which consists of 14 grid points in the El Niño basin and 193 grid points outside this domain. Following ref. 33, we consider at each node k the daily atmospheric temperature anomalies $T_k(t)$ (actual temperature value minus climatological average for each calendar day) at

Author contributions: A.B., S.H., and H.J.S. designed research; J.L., A.G., and M.I.B. performed research; A.G. and M.I.B. contributed new reagents/analytic tools; J.L. analyzed data; and A.B., S.H., and H.J.S. wrote the paper.

The authors declare no conflict of interest.

¹To whom correspondence should be addressed. E-mail: john@pik-potsdam.de.

This article contains supporting information online at www.pnas.org/lookup/suppl/doi:10.1073/pnas.1309353110/-DCSupplemental.

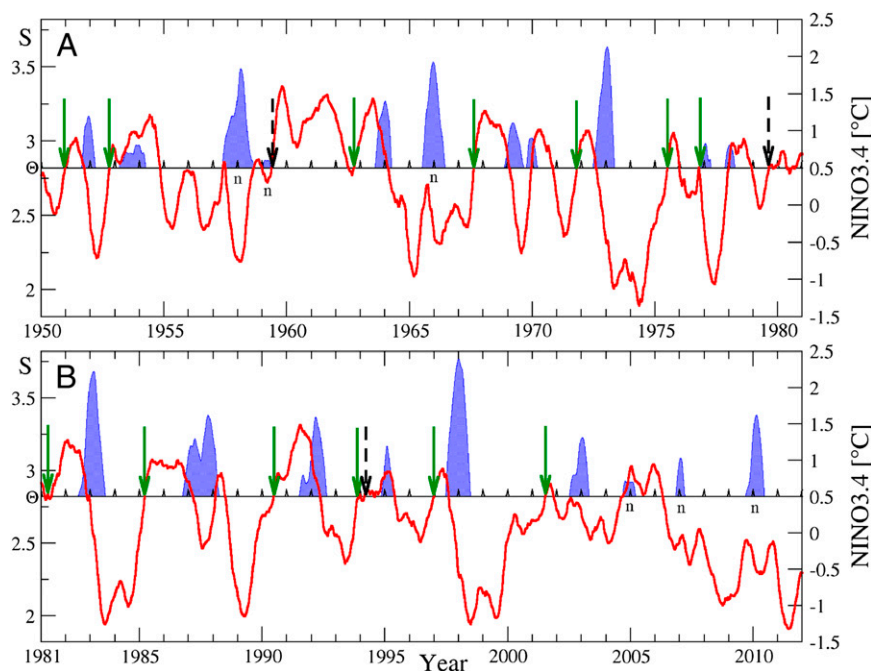


Fig. 2. The forecasting algorithm. We compare the average link strength $S(t)$ in the climate network (red curve) with a decision threshold Θ (horizontal line, here $\Theta = 2.82$) (left scale) with the standard NINO3.4 index (right scale), between January 1, 1950 and December 31, 2011. When the link strength crosses the threshold from below, outside an El Niño episode, we give an alarm and predict that an El Niño episode will start in the following calendar year. The El Niño episodes (when the NINO3.4 index is above 0.5°C for at least 5 mo) are shown by the solid blue areas. The first half of the record (A) is the learning phase where we optimize the decision threshold. In the second half (B), we use the threshold obtained in A to predict El Niño episodes. Correct predictions are marked by green arrows and false alarms by dashed arrows. The index n marks a nonpredicted El Niño episode. To resolve by eye the accurate positions of the alarms, we show in *SI Appendix, Fig. S5* magnifications of those parts of Fig. 2 where the crossings or noncrossings are difficult to see clearly without magnification. We also show the alarms for the slightly smaller threshold $\Theta = 2.81$ (*SI Appendix, Fig. S6*), which yields the same performance in the learning phase and one more false alarm in the prediction phase. The lead time between the prediction and the beginning of the El Niño episodes is 0.94 ± 0.44 y, whereas the lead time to the maximal NINO3.4 value is 1.4 ± 0.33 y.

To characterize the distribution of the best hit rates, we calculated their mean and SD. The results, also shown in Fig. 3A, are well below the hit rates achieved with the observational $S(t)$ curve.

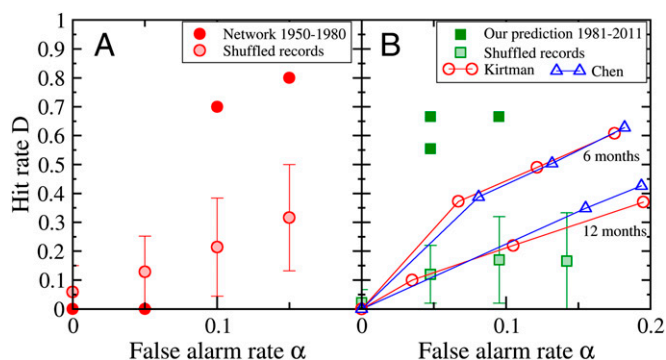


Fig. 3. The prediction accuracy [Receiver Operating Characteristic (ROC)-type analysis]. (A) For the four lowest false-alarm rates $\alpha = 0, 0.05, 0.1$, and 0.15 , the best hit rates D in the learning phase (Fig. 2A). The best results are obtained at $\alpha = 0.1$ and 0.15 . For $\alpha = 0.1$, the decision threshold Θ is between 2.805 and 2.822 . For $\alpha = 0.15$, Θ is between 2.780 and 2.792 . The results for the randomized $S(t)$ with error bars are shown as shaded circles. (B) The quality of the prediction in the second half of the record, when the above thresholds are applied. For $2.816 < \Theta \leq 2.822$, we have $D = 0.667$ at $\alpha = 0.048$; for $2.805 < \Theta \leq 2.816$, we have $D = 0.667$ at $\alpha = 0.095$; and for $2.780 < \Theta \leq 2.792$, we have $D = 0.556$ at $\alpha = 0.048$. For comparison, we show also results for 6- and 12-mo forecasts based on climate models (21, 37). The shaded squares and the error bars denote the mean hit rates and their SDs for predictions based on the shuffled data.

Next, we use the thresholds selected in the learning phase to predict El Niño episodes in the second half of the dataset between 1982 and 2011, where we have 9 episodes and 21 non-episodes. For Θ between 2.816 and 2.822 , which is depicted in Fig. 2B, the hit rate is $D = 6/9 \cong 0.667$ —at a false-alarm rate $\alpha = 1/21 \cong 0.048$. For Θ between 2.805 and 2.816 , the hit rate is also $D = 6/9$, but the false-alarm rate is $\alpha = 2/21 \cong 0.095$. For $2.780 < \Theta \leq 2.792$, we have $D = 5/9 \cong 0.556$ at $\alpha = 1/21 \cong 0.048$. These results are highly significant because the prediction efficiency is considerably better than for the shuffled data.

For comparison, we show also the results for 6- and 12-mo forecasts based on state-of-the-art climate models (21, 37). In ref. 21, an ensemble of model trajectories has been used, whereas for the forecast of ref. 37, only a single trajectory has been used. In both references, the forecast has been compared with the NINO3.4 index, as in the current analysis. Fig. 3B shows that the method suggested here for predicting El Niño episodes more than 1 y ahead considerably outperforms the conventional 6-mo and 1-y forecasts. It should be noted that although one can tune lead time and robustness in physical models, this is not possible in our statistical predictions. In contrast to physical models, which predict the SST values in the relevant regions and use them for a forecast of El Niño, our algorithm instead employs the precursors in the dynamical strength of the teleconnections in the climate network to predict the onset of the warming.

Our results suggest that for enabling local perturbations of the environment to instigate an El Niño event, the network needs to be in a “cooperative” state that can be characterized, to a certain extent, by sufficiently large link strengths in the considered climate network. The cooperativity sets in well before the spring barrier and thus allows for an early forecasting of ENSO. This

